A.W.F. Volker
Department of Acoustics & Sonar,
TNO,
The Hague 2597 AK, The Netherlands
e-mail: arno.volker@tno.nl

J.W. Vrolijk[1]
Department of Acoustics & Sonar,
TNO,
The Hague 2597 AK, The Netherlands
e-mail: jan-willem.vrolijk@tno.nl

E.J.W. Merks-Swolfs
Department of Acoustics & Sonar,
TNO,
The Hague 2597 AK, The Netherlands
e-mail: egon.merks@tno.nl

D.W. van der Burg
Department of Acoustics & Sonar,
TNO,
The Hague 2597 AK, The Netherlands
e-mail: dennis.vanderburg@tno.nl

M.S. van der Heiden
Department of Acoustics & Sonar,
TNO,
The Hague 2597 AK, The Netherlands
e-mail: maurits.vanderheiden@tno.nl

Q.E.V.N. Martina
Department of Acoustics & Sonar,
TNO,
The Hague 2597 AK, The Netherlands
e-mail: quincy.martina@tno.nl

Non-Contact MEMS-Sensor Array Inspection of Composites and Metallic Parts Using Lamb Waves

Composite materials are becoming more popular in the aerospace industry, because of their physical properties. In quality assurance and in-service inspection, there is a need for fast, non-contact, high-quality, non-destructive inspection techniques. The most common approach is to perform the inspection using water-coupled high-frequency transducers. Full wavefield techniques are promising to replace the conventional inspection approach. However, these are currently performed by a laser vibrometer setup, which has drawbacks. As an alternative, a low-cost micro-electro-mechanical system (MEMS) sensor array and dedicated processing scheme are presented enabling fast inspection of large samples. This inspection approach uses a piezoelectric actuator to excite the composite or metallic part with Lamb waves. An array of MEMS sensors records the energy that radiates into the surrounding air. A dedicated processing scheme will translate the measured wavefield into a thickness map of the inspected part. For composite parts, the material's anisotropy needs to be taken into account for accurate thickness mapping. In principle, all relevant defects show up as local thickness reductions. The results in this paper are obtained with a MEMS-sensor array of 128 elements capable of detecting ultrasound up to 250 kHz at a typical stand-off distance of 100 mm. Defects up to 6 mm in diameter could be detected in thick panels, and defects as small as 2.5 mm could be detected in thin panels. A full-size fuselage experiment shows that the method is also suited for fast inspection of large inspection areas. [DOI: 10.1115/1.4056896]

Keywords: imaging, materials testing, product quality control, sensors, ultrasonics, in-service inspection

Introduction

The application of composite materials is growing rapidly in many different industries. This is because composite materials are strong, lightweight, durable, and resistant to all kinds of weather and chemicals [1]. Moreover, composites can be used to produce complex shapes. This explains their growing popularity in many industries, such as wind turbines, aerospace, and defense. However, the use of composites in safety-critical applications requires dedicated non-destructive inspection. For these applications, all parts are 100% inspected after manufacturing [2]. The result is a plan view of multiple processed transmission or pulse-echo measurements distributed on a spatial grid [3].

Currently, these inspections are performed using high-frequency ultrasound. However, this type of inspection is generally slow and requires acoustic coupling with water, especially the squirter-based techniques. Alternatively, phased-arrays techniques could be exploited providing a high-inspection rate.

During the service life of a composite, the main risk of structural failure is caused by delamination that may occur during regular operation or due to a high energy impact [4]. According to the literature [5], no fast, high-quality, non-contact inspection method is availably capable of scanning large areas of composite materials. Conventional techniques are available but require couplant and have a very limited field of view up to only 100 mm [5].

Full wavefield techniques are of growing interest. Unlike conventional bulk wave measurements, a Lamb wave is recorded on a fully sampled spatial grid, potentially, resulting in a significant reduction in inspection time compared to conventional squirter-based techniques. Another advantage is the recording in all propagation directions, which can be exploited during data processing. The full wavefield techniques described in the literature use an expensive laser Doppler vibrometer [6–11]. Of these techniques, the processing is usually aimed at imaging the local wave amplitudes [6–9]. Flynn et al. [10] demonstrated a more effective approach which images the local wavenumber. A similar approach is described by Segers et al. [11] to image defects in stiffeners on a tail-spar panel.

In this paper, an alternative inspection approach is presented that uses low-cost micro-electro-mechanical system (MEMS) sensors [12,13] for recording instead of a scanning laser Doppler vibrometer [6–11]. The inspection approach will enable fast, non-contact inspection of, e.g., impact damage, delamination, detachment of stringers, and corrosion detection in large areas.

A custom-designed actuator is used to fill the inspection part with Lamb waves. This setup has several advantages. A MEMS-sensor array will provide a high-spatial resolution enabling to detect defects up to the required minimum diameter of about 6 mm. Compared to laser-Doppler vibrometer-based measurements, no signal averaging is required due to the high sensitivity of the MEMS sensors [14]. The sensitivity of the MEMS sensors is sufficiently high to detect the in-air radiated Lamb wave energy up to 250 kHz at a considerable stand-off distance from the surface, i.e., 100 mm or more. Compared to phased-array techniques with an aperture of 5–10 cm, the current MEMS-sensor array has a relatively large aperture of about 40 cm, which enables the inspection of

large areas in less time. Moreover, due to the low-cost sensor (typically < 1 USD), it is affordable to produce even larger arrays, which further increases inspection efficiency. Finally, the method can be applied to all relevant construction materials, i.e., metal, metal-composites, and fiber composites.

The paper is structured as follows. The processing steps involved in the non-contact inspection method are explained first. Then, the required hardware is explained in the next section, and experimental results are presented on GLARE (GLAss REinforced aluminum) and fiber composite material. After that, results on a full-size fuselage will be presented to highlight the method's potential. Finally, this paper ends with a number of conclusions.

Non-Contact Inspection Methodology

Lamb waves are introduced into a structure using a piezoelectric actuator. The frequency and local thickness determine the local wavelength. This sets the main dimensional requirements for the actuator. In principle, any Lamb wave mode can be used, provided it has sufficient out-of-plane displacement to generate a sufficiently strong signal in the air. The actuator is driven with a 2 ms linear frequency sweep to enhance the signal-to-noise ratio (SNR). This provides a sufficiently good SNR such that no further averaging of measurements is required. Furthermore, at the current operating frequency (<250 kHz), the attenuation of the A0 mode in the air is less than 0.1 dB/cm. This is negligible for the measurements described in this paper that have a stand-off distance between 100 mm and 250 mm.

The wavefield radiated from the composite panel is recorded using a MEMS-sensor array. The linear array contains 128 MEMS sensors commonly used in mobile phones or hearing aids. Although these MEMS sensors are designed to operate at audio frequencies, they still have a high sensitivity in the ultrasonic frequency band. Moreover, given their small dimensions, they are omnidirectional, and from an acoustical perspective, they can be considered point detectors. The currently used array has a sensor pitch of 3 mm, and the total aperture of the array is 384 mm. The scanning system could operate in an interleaved mode to obtain, for example, a spatial sampling of 1 mm. From a practical point of view, measurements at a relatively large stand-off distance have benefits. First, it minimizes the risk of a collision of the sensor array with the panel. Second, reflections between the sensor array and panel surface can be more easily separated from the direct wave at a larger stand-off distance.

Physically, there is a complicating factor when measuring at a non-zero stand-off distance. This originates from the fact that the phase velocity is frequency dependent. Therefore, the refraction angle is also frequency dependent according to Snell's law

$$\theta(f) = \sin^{-1} \frac{c_{air}}{c_{A0}(f)} \tag{1}$$

where θ is the angle with the normal on the surface, c_{air} is the speed of sound in air, and $c_{A0}(f)$ is the phase velocity of the Lamb wave. Consequently, based on the frequency, waves originating from the same point on the surface will be detected at different locations above the panel. In Fig. 1, a schematic is given of this physical phenomenon for an arbitrary low and high frequency.

The measured wavefield needs to be backpropagated to the surface to get rid of this refraction effect. The physical interpretation of this is that the back-propagation represents a calculation of the wavefield as it would have been measured directly at the surface. In order to do this, the MEMS-sensor array scans a horizontal plane, typically at a distance of about 100 mm above the panel. The (composite) panel can, in principle, have any shape as long as its shape is known or measured simultaneously with a laser sensor for example.

If the composite panel is flat and laying in a plane parallel to the scan plane, the back-propagation can efficiently be done in the wavenumber frequency domain [15] by multiplication with
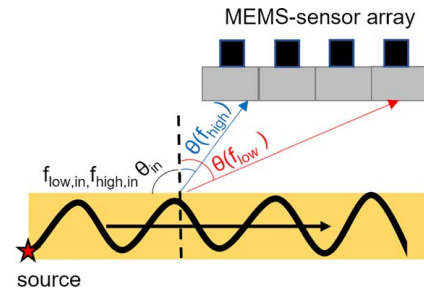
$$e^{ik_z \Delta z} \tag{2}$$

Fig. 1 The physical principle of the relation between the frequency-dependent refraction angle and the detection position on the MEMS-sensor array

where $k_z = \sqrt{\left(\frac{\omega}{c}\right)^2 - k_x^2 - k_y^2}$. The angular frequency is denoted by ω, c is the speed of sound in air, and Δz is the distance between the two planes. The horizontal wavenumbers in the x- and y-directions are indicated by k_x and k_y, respectively

The Rayleigh II integral must be used if the composite panel is not flat or non-parallel with the scan plane. In this case, the pressure in point A at the surface ($P(x_A, y_A, z_0, \omega)$) can be calculated as follows [16,17]:

$$P(x_A, y_A, z_0, \omega) = \frac{1}{2\pi} \iint^P (x, y, z, \omega) \frac{1 + ikr}{r^2} \cos \varphi e^{ikr} dx dy \tag{3}$$

where $P(x, y, z, \omega)$ is the measured wavefield, r is the distance from every measurement position to point A, φ is the angle in rad between the normal at position (x, y) on the measurement plane and point A, and $k = \omega/c$.

The spatial sampling requirements must be fulfilled for proper back-propagation of the measured wavefield. As a result of Eq. (3), the required aperture of the scan area scales up with increasing stand-off distance. Moreover, the sensitivity differences between the MEMS sensors need to be corrected before back-propagation. The calibration consists of a scan in the length direction of the array, where the scan step size equals the pitch of the array. This means that each microphone in the array records the response at the same position, and these recordings, regardless of waveform complexity, should be identical for each microphone. Calculating a filter that equalizes the response of each microphone provides the required calibration to remove the inter-sensor variations. An example of the obtained calibration filter is shown in Fig. 2. The effect of applying the calibration filter to the
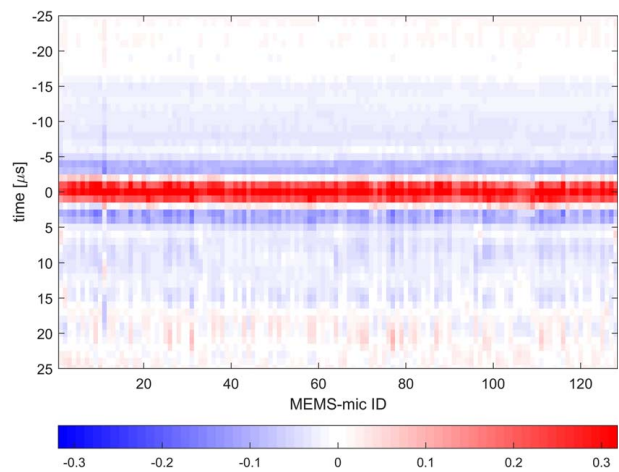

Fig. 2 An example of a calibration filter to remove inter-senor variations. Each MEMS-sensor recording is convolved with the corresponding filter.
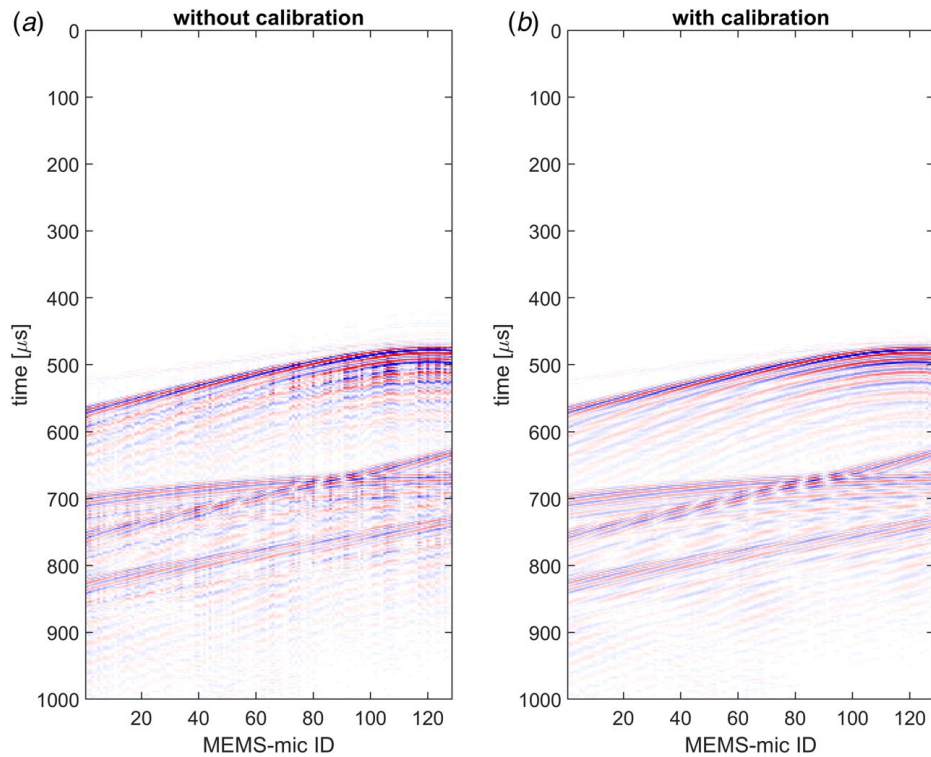
Fig. 3 Illustration of calibration process: (*a*) MEMS-sensor data before calibration and (*b*) after calibration. After calibration, the inter-sensor variations are resolved and a continuous signal is obtained.

measurements is illustrated in Fig. 3. After calibration, the coherency of the wavefield is clearly improved.

After the back-propagation of the wavefield to the surface of the composite panel, the objective is to determine the local wave velocity for a predefined set of frequencies. The wavefield is converted into a velocity map; therefore, this approach is called Direct Velocity Mapping (DVM). The direct velocity mapping (DVM) procedure is similar to estimating the local wavenumbers described by Flynn et al. [10], with the difference that, for laser Doppler vibrometer measurements, additional filtering is required to separate wave modes. This will result in separation issues and artefacts when wave modes interfere, which is not unlikely for composite materials in the low-frequency range (20–250 kHz). The measurements of a MEMS-sensor array do not require wave mode separation. The A0 mode is isolated naturally. Due to the small out-of-plane component of the S0 mode, it does not radiate in air efficiently at low thickness-frequency values.

The concept is essentially based on measuring the local wavelength for a given frequency. This allows us to calculate the local phase velocity of the wave.

Several implementations are possible, and two different classes can be discriminated:

(1) moving spatial window and
(2) band-filtering in the wavenumber domain [10].

Both approaches have been evaluated. The band-filtering approach provides superior results in terms of resolution and artifacts. The essence of the algorithm is to measure the local wavenumber (wavelength) at frequency slices from the data cube. This makes it possible to calculate a local phase velocity per frequency component.

This algorithm is repeated over a large frequency range because for a single frequency, the resulting phase velocity map may still be very noisy. A dispersion curve can either be estimated from measurements using the known nominal thickness or calculated using the fiber lay-up and the single-ply elastic properties [18–20]. In the most

general case, the dispersion curve is a function of frequency and propagation direction in case of significant anisotropy. The local thickness is obtained by mapping phase velocity to thickness. Each frequency component provides a thickness measurement, which can then be averaged to provide a thickness map of the part.

Non-Contact Inspection System

The measurement setup includes a piezoelectric actuator to introduce the Lamb waves into the composite panel and a 128-channel MEMS-sensor array to pick up the radiated wavefield from the surface.

The piezoelectric actuator was designed to be placed on most surfaces, flat or curved, and in any orientation. This is achieved by applying a vacuum pressure of less than 10 kPa to a bellow suction cup. The piezoelectric element (Meggitt A/S, DK), which has a diameter of 4 mm and thickness of 6 mm, is placed inside the suction cup adaptor. To control the contact force between the piezoelectric element and the test surface (Fig. 4),
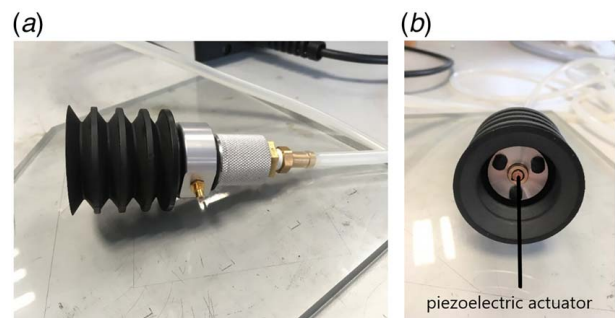

Fig. 4 Vacuum actuated Lamb source: (*a*) a side view of the actuator and (*b*) a top view of the actuator including the piezoelectric element in the middle between the three rounded bolts
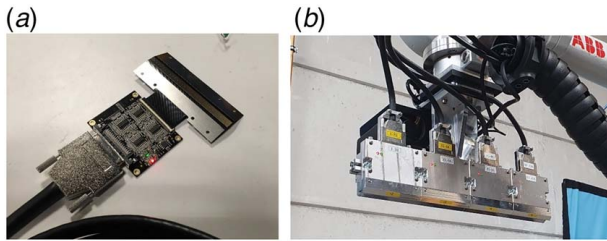
Fig. 5 An impression of the MEMS-sensor array: (a) a single module containing 32 MEMS sensors including corresponding hardware and (b) the four modules of the 128-element MEMS-sensor array mounted on an industrial robot

Table 2 Artificial defect dimensions corresponding to the GLARE 2 material in Fig. 7

Defect ID	Design diameter (mm)
1, 6, 7	3
2, 5, 8	6
3, 4, 9	12

the piezo-element is spring-loaded into a sliding subassembly structure within the adaptor. Three rounded bolts are placed in a triangular position on the front face of the adaptor to ensure stable placement of the complete actuator on the test surface. Finally, couplant was used to improve the acoustic coupling between the piezo-element and the test surface. For the experiments presented in this paper, the actuator was driven by a power amplifier and excited with a 2-millisecond linear frequency sweep containing frequencies between 20 kHz and 250 kHz at a peak-to-peak amplitude of 200 V.

The MEMS-sensor array consists of four identical modules. Each of these modules contains 32 off-the-shelf MEMS sensors. The MEMS sensors are mounted on a flexible printed circuit board (PCB, see Fig. 5(a)) with a pitch of 3 mm and are integrated into an aluminum housing or module and connected to a 128-channel analog-to-digital converter. The module housing was designed such that multiple modules can be accurately assembled next to each other, while maintaining the 3-mm microphone pitch and ensuring the correct alignment of the microphones. The whole assembly can be placed on, for example, an industrial robot (see Fig. 5(b)) or a translational system.

Experimental Results

GLARE Panel. GLARE consists of alternating layers of aluminum and prepreg. Prepreg is a fiber-filled resin. Different types of GLARE exist, with varying aluminum thickness and fiber orientation [21–23]. The used sample is a GLARE 2 with varying thickness (see Table 1); the thinnest part consists of two layers of aluminum with prepreg in between (2/1 configuration) and the thickest part is a (5/4) configuration. In Fig. 7(a), a cross-section of the material is given with a selection of Teflon inserts in each configuration. Three sets of nine artificial defects (Teflon inserts) are embedded in each configuration. The depth and diameter of these defects vary. Table 2 provides an overview of the defect sizes present in this sample.

Figure 7(b) shows a conventional ultrasonic transmission C-scan using a 5-MHz ultrasonic transducer. The detectability of the defects depends on the sample thickness; all defects in the thinnest part are detected, while most of the 2.5-mm diameter defects are difficult to detect in the thicker parts. The larger defects are clearly detected using conventional ultrasound. Figure 7(c) shows the inspection result using the DVM method. The position of the actuator on the sample is indicated by an asterisk in Fig. 7(c) and the

Table 1 Varying thickness corresponding to the GLARE 2 material in Fig. 7

Lay-up	Thickness (mm)
5/4	3.05
4/3	2.4
3/2	1.74
2/1	1.05

MEMS-sensor array records the wavefield at 100 mm above the planar side of the sample. One single dispersion curve was used to translate the measured phase velocity to a local thickness. The dispersion curve scales with the frequency-thickness product, independent of the number of aluminum–prepreg layers (see Fig. 6). The local thickness is shown in the image. In the thinnest (2/1) section, all defects are detected. In Fig. 6(c), the actual depth is given at a point location for each configuration, which is approximately ± 0.1 mm compared to the actual depth in the (4/3) and the (3/2) configurations. The difference between the actual depth is slightly larger (0.1–0.2 mm) for the (5/4) and (2/1) configurations. Figure 6(c) also gives the actual depth for the Teflon inserts from Fig. 6(a), which are approximately ± 0.1 mm compared to the measured thickness.

When the thickness increases, it becomes challenging to detect the smallest defects. Moreover, when the depth of the defect is close to the back wall, it is more difficult to detect a defect because the change in phase velocity is relatively small. This is illustrated, for example, by the relatively small phase velocity difference between the (5/4) section and the (4/4) section in Fig. 6. The thickness of the (4/4) section would be identical to the measured thickness for a defect at the last aluminum–prepreg interface. Inspecting the defect at the last aluminum-prepreg interface from the opposite side results in a lay-up at the defect location that is equivalent to the (1/0) section (see Fig. 7(a)), which has a relatively large phase velocity difference compared to the (5/4) section (see Fig. 6). Therefore, detection sensitivity of the method can be improved by two-sided inspection.

Composite Panel. Thermoplastic fiber composites are used in modern aircraft to produce the fuselage. The fiber lay-up causes the material to become anisotropic. The sample consists of carbon fiber (CF)-reinforced PolyEtherKetoneKetone (PEKK) (see Fig. 8(a)). The lay-up of this panel is [+45, −45, 90, +45, 0, −45]$_s$. Each ply has a thickness of 0.14 mm resulting in a panel thickness of 1.68 mm. The elastic properties of the material are taken from Ochoa [24]. The dispersion curve was calculated as a function of propagation direction and frequency (see Fig. 8(b)). There is clearly a measurable amount of anisotropy in the frequency range of interest, with phase velocity variations in the order of 100 m/s. The measured phase velocity is compared to a numerical 3D finite-difference modeling result, where each ply is included separately. The finite-difference scheme is based on a rotated staggered grid. In the case of anisotropy, it is known that a rotated staggered grid provides better results compared to staggered grids, where numerical artifacts are introduced because differences over boundaries are not properly taken into account [25]. The panel is built up by applying a tensor rotation related to the lay-up. The total simulation time is 120 ms, with a time sampling of about 3 ns. The vertical sampling is equal to one-fourth of the individual ply thickness, and the horizontal sampling is about 400 μm in both directions. A comparison between modeling (circle-markers) and measurement (solid line) is shown in Fig. 8(b). An excellent agreement is observed between these two results.

Measurements with the MEMS-sensor array have been performed with the panel in a convex and concave configuration. The convex shape is a typical configuration for an in-service inspection. The concave shape is typical for an inspection as part of the quality assurance process when the part is still in the mold. The
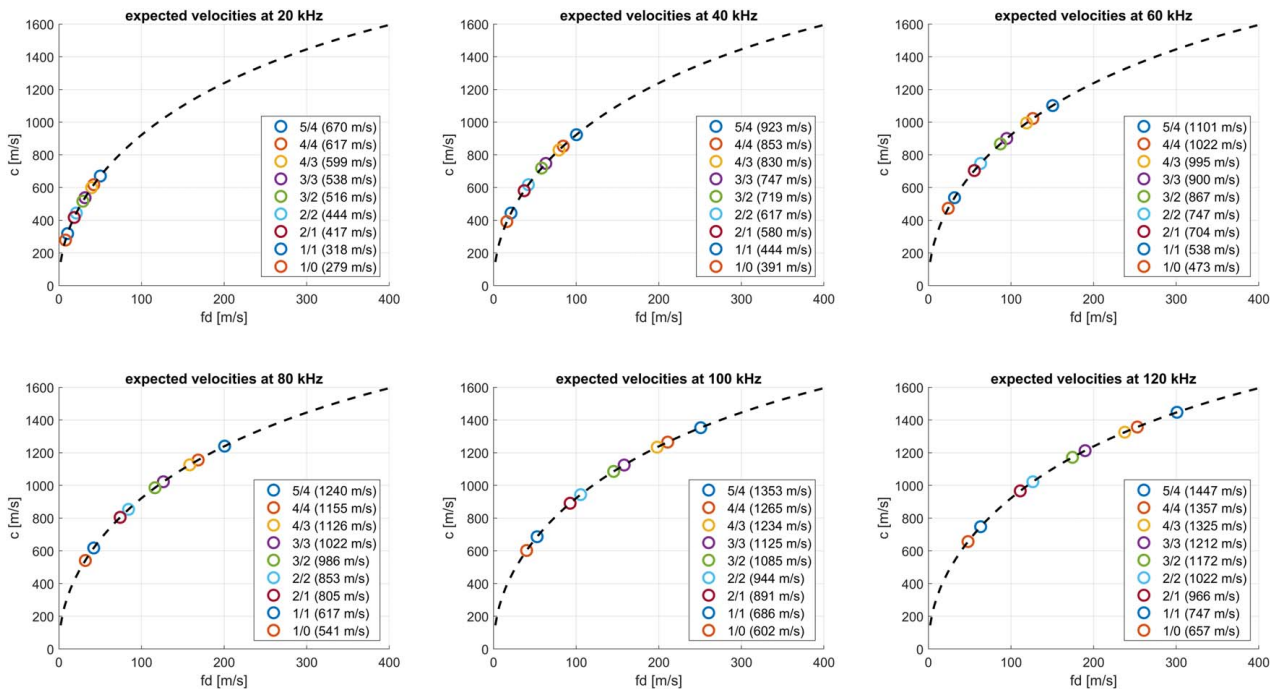
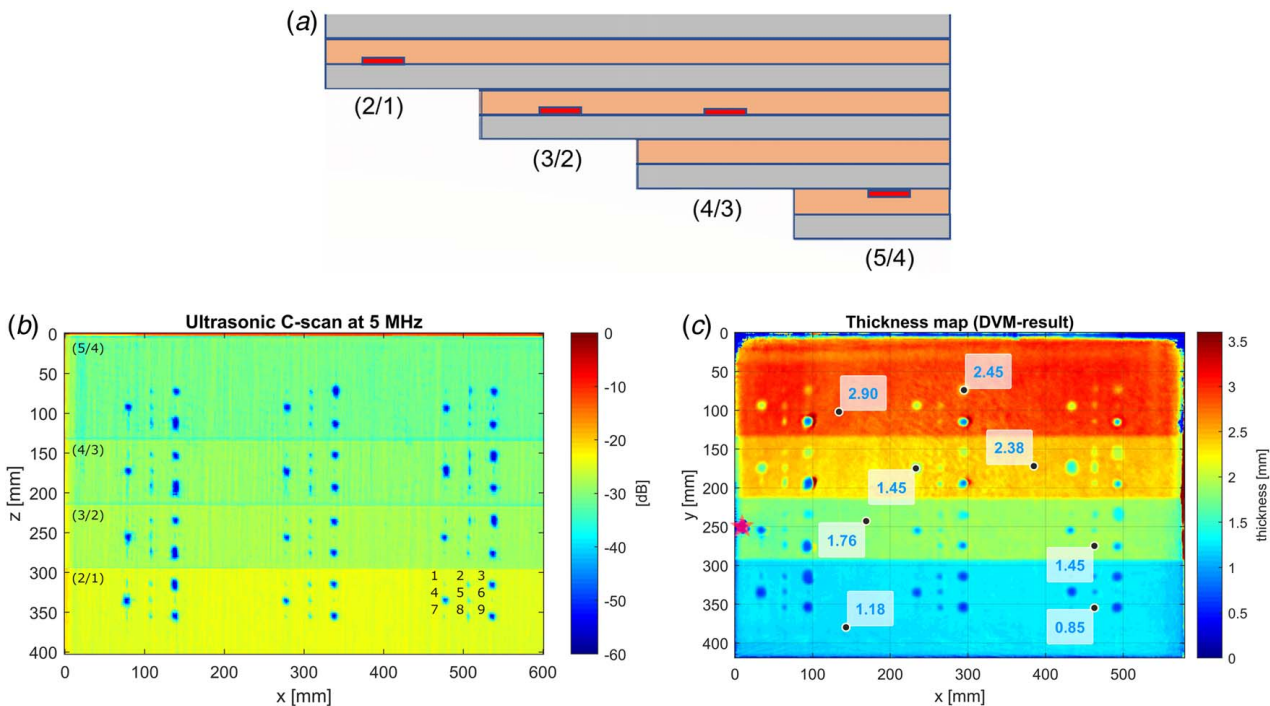**Fig. 6   Verification of scaling rule of the dispersion curve**

Fig. 7   An impression of the GLARE 2 sample and the corresponding result of two different ultrasonic techniques. (*a*) The cross-section for the GLARE 2 sample contains four different configurations. In each configuration, only a single Teflon insert is shown in each configuration (the figure is not on scale). The results of (*b*) a conventional transmission C-scan using a 5-MHz transducer and the (*c*) DVM thickness map of the GLARE 2 material. The C-scan shows the transmission amplitude on a logarithmic scale, and the thickest part has the highest attenuation. The DVM result shows the actual thickness at the depth of the defects below the surface. The values of the actual thickness at eight point locations are given including four defect locations corresponding to the defects given in Fig. 7(*a*).

actuator was positioned near the center of the panel indicated by the asterisks in Figs. 8(e) and 8(f)). The MEMS-sensor array recorded the wavefield on a planar surface at a stand-off distance of about 176 mm.

In the measured data (see time snapshot in Fig. 8(c)), the frequency and curvature (in the y-direction) dependence of the refraction angle is clearly visible. The phase velocity is extracted from the full wavefield measurement after back-propagation of the measured wavefield to the sample surface. The time snapshot in Fig. 8(d) corresponds to the wavefield from the time snapshot in Fig. 8(c) after back-propagation. The travel time difference is due to the removal of the travel time by back-propagation through air and is equal to 0.176 m/343 m/s = 513 ms by first-order approximation. After back-propagation, the effect of the curvature of the panel and frequency-dependent refraction is removed. Therefore, the ellipsoid shape (see Fig. 8(d)) indicates the anisotropic behavior of the wavefield in the panel. The wavefield measurements are processed to obtain a thickness map. The results are shown in Figs. 8(e) and

8(f) for convex and concave configurations. The nominal thickness is 1.67 mm, and the observed thickness variation within the panel is typically ± 0.2 mm.

The last example of this technique is on the application of a full-size airplane fuselage demonstrator. The demonstrator is the lower half of a full-size single-aisle aircraft. The picture in Fig. 9(a) shows a prototype inspection inside the fuselage demonstrator. The opening in the skin, shown in the back on the left side of the picture, represents the cargo door opening. Three different areas of 1 × 2 m have been inspected. During these measurements, the stand-off distance of the MEMS-sensor array was 250 mm because of the rubber wheels under the scan frame. The actuator was attached to the other side of the skin and outside the scan area. The DVM images reveal structural features of the skin lay-up, which are most pronounced around the cargo door area (see Fig. 9(c)). It is envisioned that for future applications, the array will be mounted on a large robotic arm/gantry in order to inspect the complete skin in a short
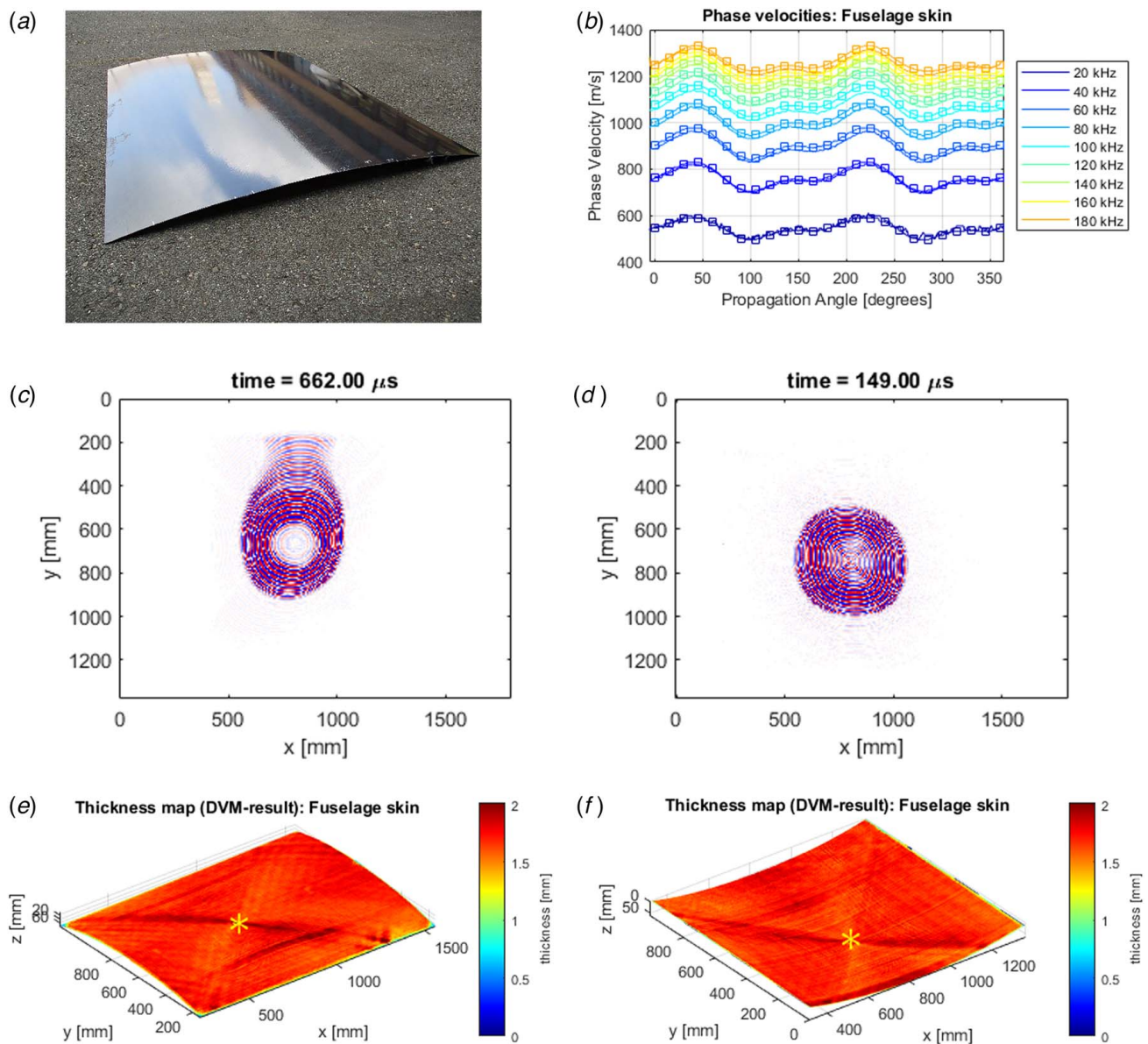

Fig. 8 Fuselage skin that has been inspected: (a) picture of the curved panel, (b) anisotropic phase velocities estimated from measurements (line) versus phase velocities from finite-difference solution (squares) for different frequencies, (c) wavefield as measured on the MEMS array, (d) backpropagated wavefield, (e) thickness map for inspection from the convex side, and (f) thickness map for inspection from the concave side
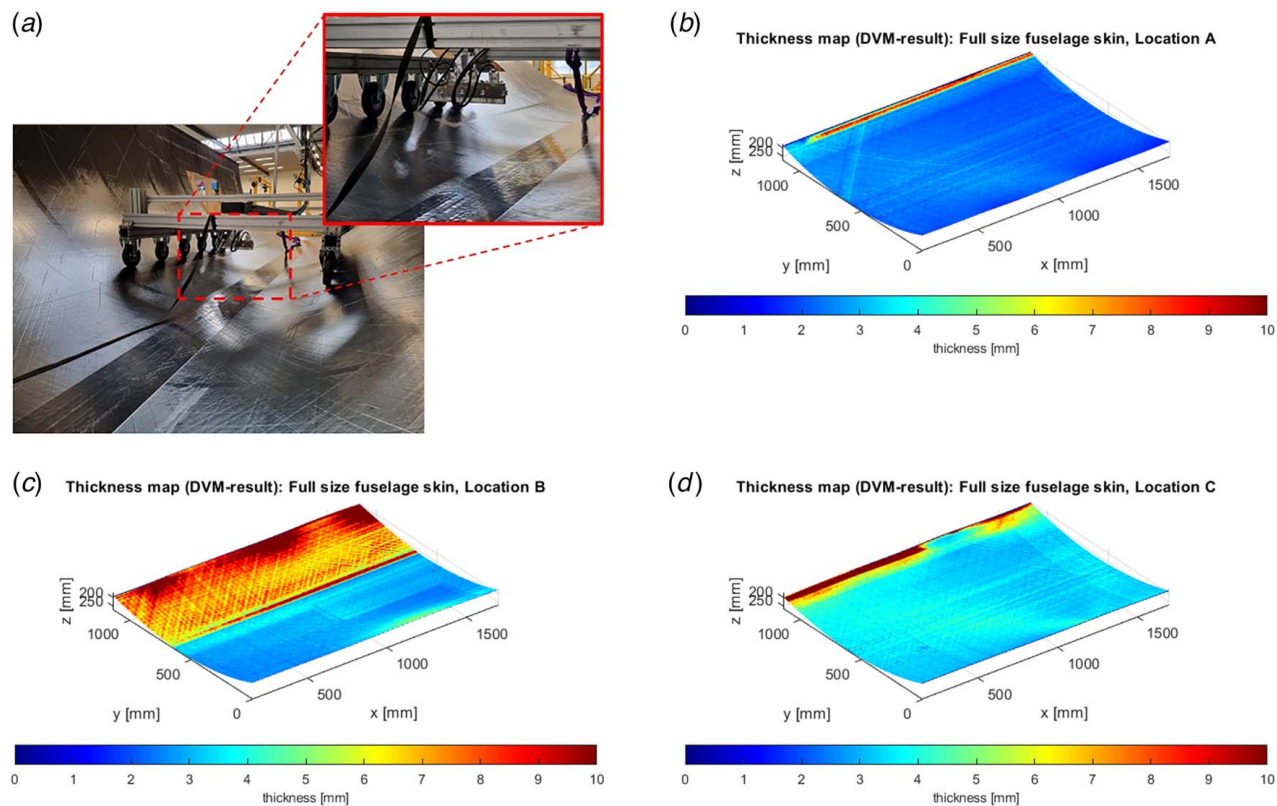
Fig. 9 An impression and results of the full-size fuselage demonstrator: (a) The setup of the full-size fuselage experiment with the MEMS-sensor array mounted on a translation scan system suspended on a trolley. The thickness maps for three different areas of the fuselage, (b) located near the edge of the cargo door, (c) located with the cargo door edge in the middle, and (d) in the center of the fuselage.

amount of time. With this technology an inspection speed of 2–5 m²/min seems feasible, making it possible to perform the inspection in substantially less time than those required by existing methods.

Conclusions

This paper presents a non-contact inspection method for metallic and composite parts using a MEMS-sensor array to record the full wavefield. The low-cost MEMS-sensor array is an alternative to conventional inspection approaches, particularly with respect to the use of expensive laser Doppler vibrometers for full wavefield measurement of large areas. All results shown have a high SNR without averaging, enabling fast scanning of large (aircraft) parts. This high SNR results from the high sensitivity of the MEMS sensors for high bandwidth (<250 kHz). Furthermore, the inter-sensor variation can easily be resolved using an appropriate calibrating filter, resulting in a high-fidelity recording system.

The MEMS-sensor array is suited for contactless inspection due to its ability to detect the leaky Lamb wave (A0 mode) in the air. The measured wavefield is translated into a thickness map of the part using a dedicated data processing scheme. The system could be mounted on an industrial robot or translational system and can operate at a large stand-off distance from the inspection material. For example, a stand-off of 250 mm was used in the full-size fuselage experiment.

In the experiments, a 128-channel MEMS-sensor array containing four 32-channel MEMS modules is used. Depending on the application-specific demands, one can choose to develop a MEMS-sensor array with more or fewer elements.

After processing, a wall thickness map is obtained. The defects show up as deviations in a local thickness map. In the processing, both isotropic and anisotropic material properties can be taken into account. The resolution of the proposed approach depends on the thickness of the inspection material. Results have shown that

defects, 6 mm in diameter, could be detected for thick panels, and defects as small as 2.5 mm could be detected for thin panels.

In conclusion, these properties make the MEMS-sensor array and data processing suitable for many quality assurance and in-service inspection applications.

Conflict of Interest

There are no conflicts of interest.

Data Availability Statement

Data provided by a third party are listed in Acknowledgment.

References

[1] Hull, D., and Clyne, T. W., 2019, *An Introduction to Composite Materials*, 3rd ed., Cambridge University Press, Cambridge.

[2] Gholizadeh, S., 2016, "A Review of Non-Destructive Testing Methods of Composite Materials," Procedia Struct. Integrity, **1**, pp. 50–57.

[3] Bond, L. J., 2018, *Nondestructive Evaluation of Materials*, Vol. 17, ASM International, Materials Park, OH.

[4] Garg, A. C., 1988, "Delamination—A Damage Mode in Composite Structures," Eng. Fract. Mech., **29**(5), pp. 557–584.

[5] Heida, J. H., and Platenkamp, D. J., 2012, "In-Service Inspection Guidelines for Composite Aerospace Structures," Proceedings of the 18th World Conference on Nondestructive Testing., Durban, South Africa, Apr. 16–20.

[6] Michaels, T. E., and Michaels, J. E., 2006, "Application of Acoustic Wavefield Imaging to Non-Contact Ultrasonic Inspection of Bonded Components," AIP Conf. Proc., **820**(1), pp. 1484–1491.

[7] Leong, W. H., Staszewski, W. J., Lee, B. C., and Scarpa, F., 2005, "Structural Health Monitoring Using Scanning Laser Vibrometry: III. Lamb Waves for Fatigue Crack Detection," Smart Mater. Struct., **14**(6), pp. 1387–1395.

[8] Lee, J.-R., Ciang Chia, C., Park, C.-Y., and Jeong, H., 2012, "Laser Ultrasonic Anomalous Wave Propagation Imaging Method With Adjacent Wave Subtraction: Algorithm," Opt. Laser Technol., **44**(5), pp. 1507–1515.

[9] Staszewski, W. J., Lee, B. C., Mallet, L., and Scarpa, F., 2004, "Structural Health Monitoring Using Scanning Laser Vibrometry: I. Lamb Wave Sensing," Smart Mater Struct., **13**(2), pp. 251–260.

[10] Flynn, E. B., Chong, S. Y., Jarmer, G. H., and Lee, J. R., 2013, "Structural Imaging Through Local Wavenumber Estimation of Guided Waves," NDT&E Int., **59**, pp. 1–10.

[11] Segers, J., Hedayastras, S., Verboven, E., Poelman, G., Van Paepegem, W., and Kersemans, M., 2019, "Full Wave Field Signal Processing Techniques for NDT of CFRP Aircraft Panel: A Case Study," Proc. Mtgs. Acoust., **38**, p. 065004.

[12] Tadigadapa, S., and Mateti, K., 2009, "Piezoelectric MEMS Sensors: State-of-the-Art and Perspectives," Meas. Sci. Technol., **20**(9), p. 092001.

[13] Lammel, G., 2015, "The Future of MEMS Sensors in Our Connected World," Proceedings of the 28th IEEE International Conference on Micro Electro Mechanical Systems (MEMS), Estoril, Portugal, Jan. 18–22, pp. 61–64.

[14] Flynn, E. B., and Jarmer, G. H., 2013, "High-Speed, Non-Contact, Baseline-Free Imaging of Hidden Defects Using Scanning Laser Measurements of Steady-State Ultrasonic Vibration," Proceedings of the Conference: 9th International Workshop on Structural Health Monitoring, Stanford, CA, Sept. 10–12.

[15] Gazdag, J., 1978, "Wave-Equation Migration by Phase Shift," Geophysics, **43**(7), pp. 1342–1351.

[16] Berkhout, A. J., 1985, *Seismic Migration, Imaging of Acoustic Energy by Wave Field Extrapolation: Theoretical Aspects*, 3rd ed., Elsevier, Amsterdam.

[17] Wapenaar, C. P. A., and Berkhout, A. J., 1989, *Elastic Wave Field Propagation: Redatuming of Single- and Multi-Component Seismic Data*, Elsevier, Amsterdam.

[18] Knopoff, L., 1964, "A Matrix Method for Elastic Waves Problems," Bull. Seismol. Soc. Am., **54**(1), pp. 431–438.

[19] Pavlakovic, B., and Lowe, M., 2003, *DISPERSE Manual*, Imperial College London, London.

[20] Pant, S., Laiberte, J., Martinez, M., and Rocha, B., 2024, "Derivation and Experimental Validation of Lamb Wave Equations for an n-Layered Anisotropic Composite Laminate," Compos. Struct., **111**, pp. 566–579.

[21] Wu, G., and Yang, J. M., 2005, "The Mechanical Behavior of GLARE Laminates for Aircraft Structures," JOM, **57**(1), pp. 72–79.

[22] Gusev, A. A., Hine, P. J., and Ward, I. M., 2005, "Fiber Packing and Elastic Properties of a Transversely Random Unidirectional Glass/Epoxy Composite," Compos. Sci. Technol., **60**(4), pp. 535–541.

[23] Vlot, A., and Gunnik, J. W., 2011, *Fiber Metal Laminates: An Introduction*, Springer, Dordrecht.

[24] Ochôa, P., 2019, "Ultrasonic Health Monitoring of Thermoplastics Composite Aircraft Primary Structures," Doctoral dissertation, Delft University of Technology.

[25] Saenger, E. H., and Bohlen, T., 2004, "Finite-Difference Modeling of Viscoelastic and Anisotropic Wave Propagation Using the Rotated Staggered Grid," Geophysics, **69**(2), pp. 583–591.